Journal of Catalysis 440 (2024) 115779

Contents lists available at ScienceDirect

Journal of Catalysis

journal homepage: www.elsevier.com/locate/jcat

# Hydrogen activation by rhodium under the cover of a copper oxide thin film

Volkan Çınar [a], Eva Peurrung [b], Hojoon Lim [c], Adrian Hunt [c], Maggie Rickman [b], Grace Miller [b], Jean-Sabin McEwen [b,d,e,f,g,*], E. Charles H. Sykes [a,**], Iradwikanari Waluyo [c,***]

[a] Department of Chemistry, Tufts University, Medford, MA 02155, United States
[b] The Gene and Linda Voiland School of Chemical Engineering and Bioengineering, Washington State University, WA 99164, United States
[c] National Synchrotron Light Source II, Brookhaven National Laboratory, Upton, NY 11973, United States
[d] Department of Physics and Astronomy, Washington State University, Pullman, WA 99164, United States
[e] Department of Chemistry, Washington State University, Pullman, WA 99164, United States
[f] Institute for Integrated Catalysis, Pacific Northwest National Laboratory, Richland, WA 99352, United States
[g] Department of Biological Systems Engineering, Washington State University, Pullman, WA 99164, United States

ARTICLE INFO

*Keywords:*
Rhodium
Copper oxide
Single-atom catalysis
Hydrogen activation
Metal-oxide interfaces

ABSTRACT

The activation of reactants by catalytically active metal sites at metal-oxide interfaces is important for understanding the effect of metal-support interactions on nanoparticle catalysts and for tuning activity and selectivity. Using a combined experimental and theoretical approach, we studied the activation of $H_2$ and the effect of CO poisoning on isolated Rh atoms completely or partially covered by a copper oxide ($Cu_2O$) thin film. Temperature-programmed desorption (TPD) experiments conducted in ultra-high vacuum (UHV) show that neither a partially nor a fully oxidized $Cu_2O$ layer grown on a Rh/Cu(111) single-atom alloy can activate hydrogen in UHV. However, in situ ambient pressure X-ray photoelectron spectroscopy (AP-XPS) experiments performed at elevated $H_2$ pressures reveal that Rh significantly accelerates the reduction of these $Cu_2O$ thin films by hydrogen. Remarkably, the fastest reduction rate is observed for the fully oxidized sample with all Rh sites covered by $Cu_2O$. Both TPD and AP-XPS data demonstrate that these covered Rh sites are inaccessible to CO, indicating that Rh under $Cu_2O$ is active for $H_2$ dissociation but cannot be poisoned by CO. In contrast, an incomplete oxide film leaves some of the Rh sites exposed and accessible to CO, and hence prone to CO poisoning. Density functional theory calculations demonstrate that unlike many reactions in which hydrogen *activation* is rate limiting, the rate-determining step in the dissociation of $H_2$ on thin-film $Cu_2O$ with Rh underneath is the *adsorption* of $H_2$ on the buried Rh site, and once adsorbed, the dissociation of $H_2$ is barrierless. These calculations also explain why $H_2$ can only be activated at higher pressures. Together, these results highlight how different the reactivity of atomically dispersed Rh in Cu can be depending on its accessibility through the oxide layer, providing a way to engineer Rh sites that are active for hydrogen activation but resilient to CO poisoning.

## 1. Introduction

Hydrogenation is a critical chemical reaction for many processes in the food, pharmaceutical and petrochemical industries such as hydrogenation of vegetable oils [1], asymmetric hydrogenation [2,3], hydrocracking [4,5], and catalytic reforming [6]. In addition, hydrogenation reactions are heavily relied on to convert unsaturated alkenes into saturated alkanes and convert $CO_2$ to higher value products [7–9]. Typically, heterogeneous catalysts involving oxide-supported transition metals (Pd, Ni, Ru, Rh, Pt) are used for hydrogenation processes industrially [10–14]. However, these catalysts are often prone to deactivation by sintering [15–17], coking [18,19], and poisoning [20,21]. To overcome the deactivation issue for hydrogenation catalysis, single-atom catalysts (SACs) consisting of active metal dopants

* Corresponding author at: The Gene and Linda Voiland School of Chemical Engineering and Bioengineering, Washington State University, WA 99164, United States.
** Corresponding author at: Department of Chemistry, Tufts University, Medford, MA 02155, United States.
*** Corresponding author at: National Synchrotron Light Source II, Brookhaven National Laboratory, Upton, NY 11973, United States.
*E-mail addresses:* js.mcewen@wsu.edu (J.-S. McEwen), charles.sykes@tufts.edu (E.C.H. Sykes), iwaluyo@bnl.gov (I. Waluyo).

https://doi.org/10.1016/j.jcat.2024.115779
Received 31 May 2024; Received in revised form 6 September 2024; Accepted 27 September 2024
Available online 28 September 2024

atomically dispersed on supports have been extensively investigated of late [22–28].

SACs have the added advantages of offering high selectivity due to their uniform active sites while minimizing the use of precious metals. Oxide-supported SACs can be susceptible to deactivation due to strong metal-support interaction (SMSI) where the oxide migrates to the surface and covers the active metal sites, potentially hindering $H_2$ activation [29–31]. Consequently, there have been several efforts to study the reaction kinetics and surface chemistry of metal sites covered by an oxide overlayer, and in confined pores, to understand how the metal-support interaction affects catalytic activity [32–37] for the diffusion, activation, and spillover of hydrogen [38]. In one study, Pt was found to promote the diffusion and spillover of hydrogen on a manganese oxide overlayer, but $H_2$ dissociation required the presence of bare Pt sites [39]. In another study, Prieto *et al.* demonstrated that Ru(0001) covered by a crystalline $SiO_2$ bilayer has a decreased apparent activation energy of 0.32 eV for the water formation reaction compared to the value of 0.59 eV for uncovered Ru(0001) [40]. The authors theorized that the decrease was due to the reaction becoming diffusion-controlled under confinement. Through their theory work, the authors concluded that although the rate-determining step for both confined and unconfined systems is the formation of surface hydroxyls, the $H_2$ adsorption step plays a key role in the overall reaction kinetics. In addition, the authors hypothesized that the position of the silica bilayer with respect to the ruthenium surface plays a key role in the formation of water [40].

In this study, we used a well-defined copper oxide ($Cu_2O$) thin film model oxide support. It is known that at elevated pressures, $H_2$ activation on $Cu_2O$-based systems results in the reduction of the $Cu_2O$ to metallic Cu through the formation of $H_2O$ [41,42]. However, $H_2$ dissociation on pristine $Cu_2O$ has a high activation energy, preferentially occurring on step edges and defects, resulting in a slow oxide reduction rate with a long induction period at room temperature [41–44]. Using a combination of ambient pressure X-ray photoelectron spectroscopy (AP-XPS), temperature-programmed desorption (TPD), and density functional theory (DFT) calculations, we previously reported that doping $Cu_2O$ with a dilute amount of Pt, such as by preparing the oxide from a PtCu single-atom alloy (SAA), promotes $H_2$ dissociation and accelerates the reduction rate of the oxide [45]. We found that when Pt sites are covered by a complete oxide layer, they are blocked from $H_2$ adsorption and dissociation, but the Pt atoms still indirectly promote the reduction of $Cu_2O$ by weakening nearby Cu–O bonds.

In this work, we studied analogous $Cu_2O$ thin film surfaces prepared from the RhCu(111) SAA in order to evaluate the role of Rh sites under the oxide in activating $H_2$. TPD results indicate that $H_2$ dissociation does not occur under ultra-high vacuum (UHV) exposure conditions on $Cu_2O$ thin films or those with Rh atoms underneath. However, AP-XPS demonstrates that a continuous exposure to near-ambient pressure $H_2$ at room temperature results in a significantly accelerated reduction of the Rh-doped oxide compared to the undoped oxide. We found that unlike Pt, Rh sites covered by a layer of $Cu_2O$ are accessible to $H_2$ adsorption at elevated pressures and play a direct role in $H_2$ activation, which results in the rapid reduction of the oxide layer. However, when the oxide layer is incomplete or defective, exposed Rh sites are prone to deactivation due to CO poisoning, which decreases the number of active sites for $H_2$ dissociation and consequently slows the reduction rate of the oxide layer. Results from DFT calculations confirm that the dissociative adsorption of $H_2$ is activated, and thus if the pressure is low enough, such as when one is under UHV conditions, the dissociative adsorption of $H_2$ will not readily occur. However, at high enough pressures, the relatively low activation barrier can be overcome, and the reduction of the oxide can proceed. This study shows how the reactivity of a catalyst toward hydrogen activation can be tuned by modifying the metal-oxide interface.

## 2. Experimental and Computational Methods

### 2.1. Temperature-Programmed desorption (TPD)

TPD studies were performed using a UHV chamber with a base pressure of lower than $1 \times 10^{-10}$ Torr using a Hiden Hal RC 201 mass spectrometer which could be approached to ~1 mm from the sample face. The Cu(111) single crystal sample could reach cryogenic temperatures (~85 K) using liquid nitrogen cooling and could be heated to 750 K via resistive heating of the tungsten support wires. The Cu(111) crystal was cleaned using several $Ar^+$ bombardment cycles (~2 μA drain current, 1.5 kV) and annealing to 750 K. RhCu SAA was made by depositing Rh from an Omicron EFM 3 electron beam evaporator onto the Cu(111) crystal at 383 K. One monolayer of Rh is defined relative to the packing density of Cu(111), $1.77 \times 10^{15}$ atoms•cm$^{-2}$. Cu(111) and the RhCu SAA were exposed to $4 \times 10^{-6}$ Torr of isotopic $^{18}O_2$ (99%, Aldrich) at 400 K for either 3 min or 20 min to form the $Cu_2O$(3min) or the $Cu_2O$ (20min), respectively. The oxidized RhCu SAA surfaces are hereafter referred to as Rh/$Cu_2O$(3min) and Rh/$Cu_2O$(20min). For the oxidized surfaces, saturation isotopic $^{13}CO$ (99%, Aldrich), $H_2$ (99.9%, Airgas), and $D_2$ (99.9%, Sigma-Aldrich) were exposed to the crystal at 90 K. For the case of RhCu SAA, $H_2$ was exposed at 200 K. TPDs were performed with a linear heating rate of 1 K/s.

### 2.2. Ambient pressure X-ray photoelectron spectroscopy (AP-XPS)

AP-XPS experiments were conducted at the In situ and Operando Soft X-ray spectroscopy (IOS, 23-ID-2) beamline at the National Synchrotron Light Source II (NSLS-II), Brookhaven National Laboratory. A detailed technical description about the beamline and endstation capabilities can be found in another publication [46]. Cu(111) was cleaned using repeated cycles of $Ar^+$ sputtering and annealing to 850 K. Sample heating was achieved using a pyrolytic boron nitride heater and the temperature was read using a type K thermocouple placed between the crystal and the heater. The RhCu SAA was prepared by depositing 1% Rh onto Cu(111) at 370–380 K using a SPECS EBE-4 electron beam evaporator calibrated using a quartz crystal microbalance. Cu(111) and the RhCu SAA were oxidized by exposing the sample to $5 \times 10^{-6}$ Torr of $O_2$ (99.994%, Matheson) at 400 K for either 3 min or 20 min. Cu 2*p* spectra of the Cu(111) and RhCu(111) surface after oxidation for 20 min confirm the presence of $Cu_2O$ in the $Cu^{1+}$ oxidation state (Figure S1). During AP-XPS experiments, CO (99.999%, Matheson) and $H_2$ (99.999%, Matheson) were introduced into the chamber using high precision variable leak valves. The gas pressure was read using a combination Pirani and hot cathode ion gauge below 1 mTorr and a capacitance manometer for better accuracy above 1 mTorr. Experiments in ambient pressure of $H_2$ were performed with a detuned undulator to reduce the photon flux and eliminate beam-induced effects. The O 1*s* core level was acquired using a photon energy of 710 eV, while Rh 3*d* and C 1*s* core levels were measured using a photon energy of 500 eV. The Fermi edge was measured at each photon energy and was used for binding energy calibration.

### 2.3. Density functional theory calculations

All DFT simulations were conducted using the Vienna Ab initio Simulation Package (VASP) software [47,48]. The Gaussian method of electron smearing was used with a smearing width of 0.2 eV. Geometric optimizations were considered converged when the total energy changed by less than $1 \times 10^{-6}$ eV and interatomic forces were less than 0.03 eV/Å. The core electrons were described using the projector augmented wave (PAW) method [49,50] that were released in 2015 [51]. The valence electrons were modeled using a plane-wave basis set with a cutoff energy of 500 eV. The exchange–correlation potential was modeled with the Perdew-Burke-Ernzerhof functional [52]. Structural visualizations were performed with OVITO [53].

For hydrogen dissociation calculations, the "29" $Cu_xO$ model was used. In this model, the bulk lattice constant was optimized to be 3.635 Å. More details on the construction of this surface are described in our previous work [54–56]. Various locations of Rh in the "29" $Cu_xO$ hollow site were tested, which involved either a single atom under the oxide or a cluster of atoms under the oxide. The structures involving Rh under the oxide were created by replacing bulk Cu atoms with Rh and performing a geometry relaxation. All calculations were performed using a (1 × 2 × 1) Monkhorst-Pack grid and the bottom two layers were fixed to simulate bulk copper. Transition states were found using the climbing image nudged elastic band (CI-NEB) method with the same convergence criteria used in geometric optimizations [57,58]. Transition states were verified by calculating the vibrational modes and ensuring that there was one imaginary mode along the reaction pathway [59].

## 3. Results and Discussion

### 3.1. Experimental results – TPD and AP-XPS

We used TPD to investigate the reactivity of $Cu_2O$ surfaces with and without Rh doping toward $H_2$ dissociation. Briefly, the "29" $Cu_2O$ is a single layer thin film oxide grown on a Cu(111) surface and it consists of hexagonal rings with six oxygen and six copper atoms. The unit cell of the "29" $Cu_2O$ is believed to contain six of these hexagonal rings with five of them containing an oxygen adatom at the center [56,60–62]. The $Cu_2O$ used in this work was prepared by decreasing the oxidation temperature of the Cu(111) crystal from the typical 650 K used to prepare the "29" $Cu_2O$ to 400 K. The lower oxidation temperature was necessary to prevent the diffusion of Rh atoms into the Cu bulk. Rh/$Cu_2O$(3min) and Rh/$Cu_2O$(20min) were prepared by first depositing a low coverage of Rh on a Cu(111) surface to prepare a RhCu SAA surface, followed by oxidation at 400 K for either 3 min or 20 min. While the exact structures of the $Cu_2O$(3min) and $Cu_2O$(20min) surfaces are unknown, published LEED patterns are noticeably different than that of the "29" $Cu_2O$ and each other [45]. $H_2$ dissociation on the RhCu SAA surface was used as a control experiment since it is active for $H_2$ dissociation as can be seen by the $H_2$ recombinative desorption peak observed at ~280 K shown in the TPD data in Fig. 1. On the other hand, no recombinative $H_2$ desorption peaks were observed for the both the Rh/$Cu_2O$(3min) and Rh/$Cu_2O$(20min) surfaces, similar to the control experiment on an undoped $Cu_2O$(3min) surface, which indicates that these surfaces cannot activate $H_2$ under these experimental conditions. This is a different behavior from the 3-min oxidized PtCu SAA, which was previously reported to be active in $H_2$ dissociation due to the presence of exposed Pt sites not covered by oxide after the shorter 3-min oxidation time [45].

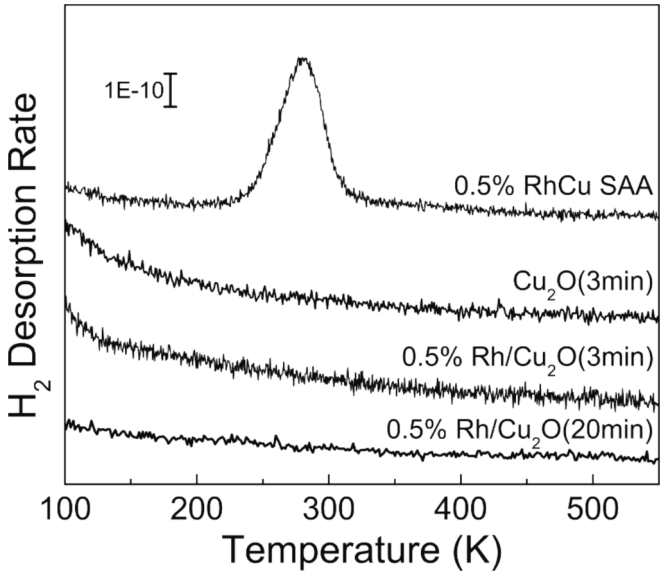


**Fig. 1.** $H_2$ desorption TPD experiments from 0.5% RhCu SAA, bare $Cu_2O$ (3min), 0.5% Rh/$Cu_2O$(3min), and 0.5% Rh/$Cu_2O$(20min). To make the oxide surfaces, Cu(111) or the RhCu(111) SAA were exposed to 4 × $10^{-6}$ Torr $O_2$ pressure at 400 K for 3 or 20 min. 100 L of $H_2$ was then exposed to the oxidized surfaces at 90 K and to the RhCu SAA at 200 K.

Next, we studied $H_2$ dissociation at near-ambient pressure conditions using AP-XPS to simulate more realistic hydrogenation conditions under which the catalyst was continuously exposed to $H_2$ gas. An undoped $Cu_2O$(3min) surface was used as the control experiment, and Rh/$Cu_2O$ surfaces were prepared by oxidizing a 1% RhCu SAA surface using the same conditions as the TPD experiments. The surfaces were then exposed to 1 Torr of $H_2$ at 300 K and the O 1*s* spectra were continuously acquired every 35 s in the presence of $H_2$ to monitor the changes in the oxide peak as the reduction reaction progressed. We also compared the effect of Rh to that of Pt with the same initial coverage of the dopant metal.

Fig. 2 shows the plots of the O 1*s* oxide peak area as a function of $H_2$ exposure time with Pt (Fig. 2A) and Rh (Fig. 2B) dopants. As expected, the reduction of pristine $Cu_2O$(3min) (black squares) proceeds slowly due to the high activation energy for $H_2$ dissociation on the $Cu_2O$ surface

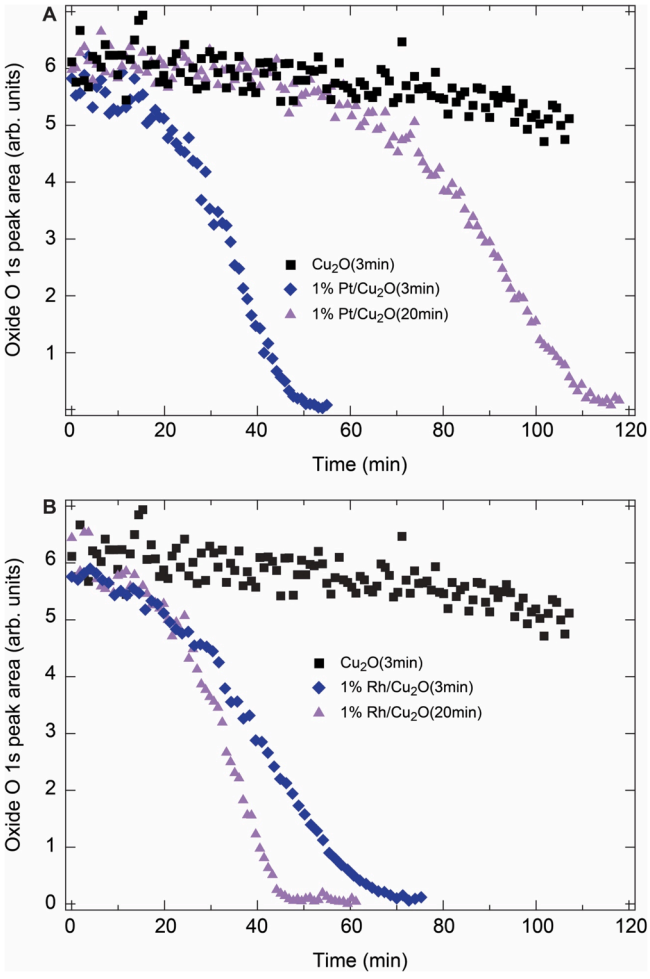


**Fig. 2.** AP-XPS-derived plots of oxide O 1*s* peak area as a function of exposure time to 1 Torr of $H_2$ at 300 K for (A) 1% Pt/$Cu_2O$ surfaces prepared by oxidizing PtCu SAA for 3 min (blue diamonds) and 20 min (purple triangles) compared to the pristine $Cu_2O$(3min) surface (black squares), and (B) 1% Rh/$Cu_2O$ surfaces prepared by oxidizing RhCu SAA for 3 min (blue diamonds) and 20 min (purple triangles) compared to the pristine $Cu_2O$ surface (black squares). O 1*s* spectra were acquired every 35 s at a photon energy of 710 eV.

[41–43]. The reduction rate is enhanced by the presence of both Pt and Rh. For the Pt/$Cu_2O$ surfaces (Fig. 2A), Pt/$Cu_2O$(3min) (blue diamonds) is reduced much more rapidly than Pt/$Cu_2O$(20min) (purple triangles), consistent with the previously published results for different initial coverages of Pt [45]. The accelerated reduction of the Pt/$Cu_2O$(3min) surface is attributed to facile $H_2$ dissociation on exposed Pt sites due to the formation of an incomplete oxide film [45]. In contrast, for the Pt/$Cu_2O$(20min) sample, the Pt atoms are covered by a complete oxide film and they are not able to dissociate $H_2$. This results in a long (~60 min) induction period as the slow first step of reduction, followed by a more rapid second step that commences after some Pt sites become exposed and active for $H_2$ dissociation, as seen in Fig. 2A. Interestingly, the Rh/$Cu_2O$ surfaces (Fig. 2B) show a completely different reduction behavior in $H_2$. Specifically, the Rh/$Cu_2O$(20min) surface has a significantly shorter induction period than the analogous Pt/$Cu_2O$(20min) surface, and in fact, the reduction of the more oxidized Rh/$Cu_2O$(20min) sample proceeds slightly faster than the less oxidized Pt/$Cu_2O$(3min) system. In addition, a less dramatic difference is observed between the Rh/$Cu_2O$(3min) and Rh/$Cu_2O$(20min) surfaces, and even more interestingly, the former is reduced more slowly than the latter, which is the opposite of the case with Pt.

To understand this unexpected reduction behavior of the Rh/$Cu_2O$ system, we used adsorbed CO as a probe to identify the accessibility of the Rh sites relative to their location, *on* vs *under*, the oxide layer and to gain more insight into the role of the Rh sites for $H_2$ dissociation. Fig. 3 shows the Rh $3d_{5/2}$ and C 1*s* spectra of the metallic and oxidized RhCu surfaces before and after exposure to $1 \times 10^{-4}$ Torr of CO for 30 s. Oxidized rhodium species has a Rh $3d_{5/2}$ binding energy range of 308–310 eV [63–65]. Based on the Rh $3d_{5/2}$ spectra of both 3-min and 20-min oxidized samples compared to the as-deposited Rh/Cu(111) sample (Fig. 3A), Rh remains in the metallic state. The brief exposure to low pressure of CO at 300 K does not result in detectable changes to the oxide peak. As shown in the top spectra for the metallic RhCu SAA surface, CO adsorption on Rh sites manifests as a shift of the Rh $3d_{5/2}$ peak to a higher binding energy due to the formation of Rh-CO bond, as well as the appearance of the C 1*s* peak at ~286.2 eV arising from adsorbed CO. The C 1*s* peak at ~284.2 eV is from carbon contamination that appeared on the surface after Rh deposition, and it does not play a role in oxidation or reduction. The middle spectra show Rh/$Cu_2O$(3min) at 300 K before (solid dark blue) and after (dotted light blue) CO exposure. The slight shift in the Rh $3d_{5/2}$ peak to higher binding energy and the C 1*s* peak at ~286.2 eV confirm the presence of adsorbed CO on the small amount of exposed Rh sites present after the 3-minute oxidation. However, an adsorbed CO peak in the C 1*s* region is already observed for this surface even before the introduction of CO to the system, and this CO peak has approximately half of the intensity of the peak after CO exposure. This suggests that at 300 K, at least half of the exposed Rh sites remaining after the 3-minute oxidation already have adsorbed CO from the UHV chamber background. By comparing the peak area of adsorbed CO on the Rh/$Cu_2O$(3min) surface to that on the metallic RhCu SAA surface, assuming a saturation coverage of CO on surface Rh sites, we estimate that ~20% of the initial surface Rh sites are still exposed after the 3-minute oxidation. For the Rh/$Cu_2O$(20min) surface (bottom spectra), both C 1*s* and Rh $3d_{5/2}$ spectra show no evidence of adsorbed CO either before or after CO exposure, indicating the absence of exposed Rh sites in the more oxidized Rh/$Cu_2O$(20min) sample, similar to Pt/$Cu_2O$(20min) in which all the Pt atoms are buried by the oxide layer [45].

After understanding the accessibility of the CO adsorption sites in these different systems, we probed their activity for CO oxidation with TPD. When small amounts of Rh are deposited on the "29" $Cu_2O$ surface, molecularly adsorbed CO is fully converted to $CO_2$ upon heating the sample [66]. In contrast, CO oxidation does not occur on the undoped $Cu_2O$(3min) surface, as shown by the absence of a $CO_2$ desorption peak in the upper trace of Fig. 4A. Therefore, the desorption of $CO_2$ provides evidence for the presence of exposed Rh sites, which are known to be active for CO oxidation [66]. For the 0.5% Rh/$Cu_2O$(3min) sample, which was prepared by oxidizing a RhCu SAA instead of depositing Rh on $Cu_2O$, the surface is active for CO oxidation as evidenced by the $CO_2$ desorption peak at ~450 K shown in the middle trace of Fig. 4A. Isotopic substitution experiments by preparing the $Cu_2O$ surface with $^{18}O_2$ and exposing it to $^{13}C^{16}O$ enabled us to definitively identify the source of the desorbed $CO_2$, shown in Fig. 4B. The presence of a $^{13}C^{16}O^{18}O$ peak (lower TPD trace in Fig. 4B) indicates that adsorbed $^{13}C^{16}O$ reacts with an $^{18}O$ atom from the oxide surface through the Mars van Krevelen (MvK) mechanism [66]. On the other hand, the $^{12}C^{16}O^{18}O$ peak (upper trace in Fig. 4B) is due to background $^{12}C^{16}O$ in the chamber adsorbing to the Rh sites and similarly oxidized through the MvK mechanism to form $^{12}C^{16}O^{18}O$. This supports our interpretation of the XPS data that after the 3-minute oxidation, some of the Rh sites are accessible to CO adsorption (including background CO) because they are not completely covered by the oxide layer due to the formation of an incomplete/

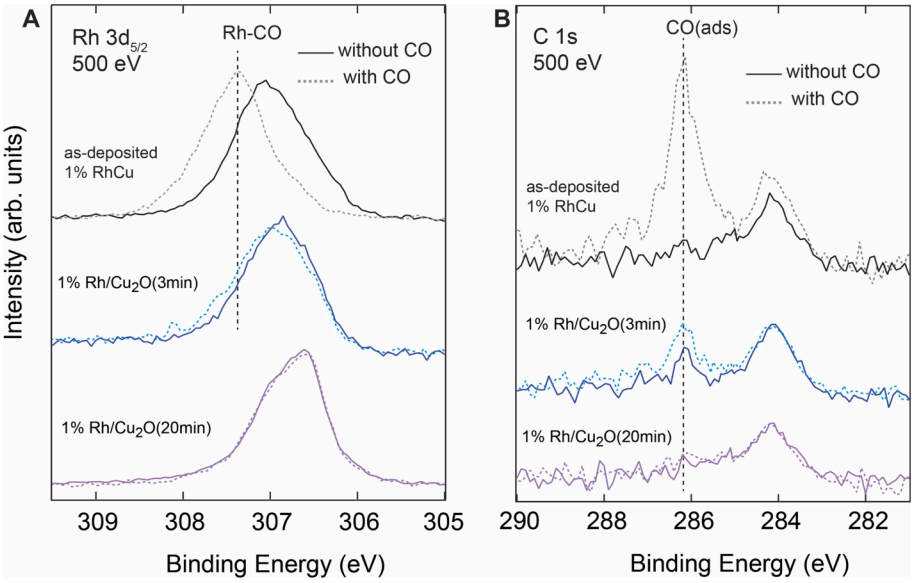


**Fig. 3.** (A) Rh $3d_{5/2}$ and (B) C 1*s* core level XPS spectra of the as-deposited 1% RhCu SAA (top), 1% Rh/$Cu_2O$(3min) surface (middle), and 1% Rh/$Cu_2O$(20min) surface (bottom) before (solid lines) and after (dotted lines) exposure to $1 \times 10^{-4}$ Torr of CO for 30 s at 300 K.

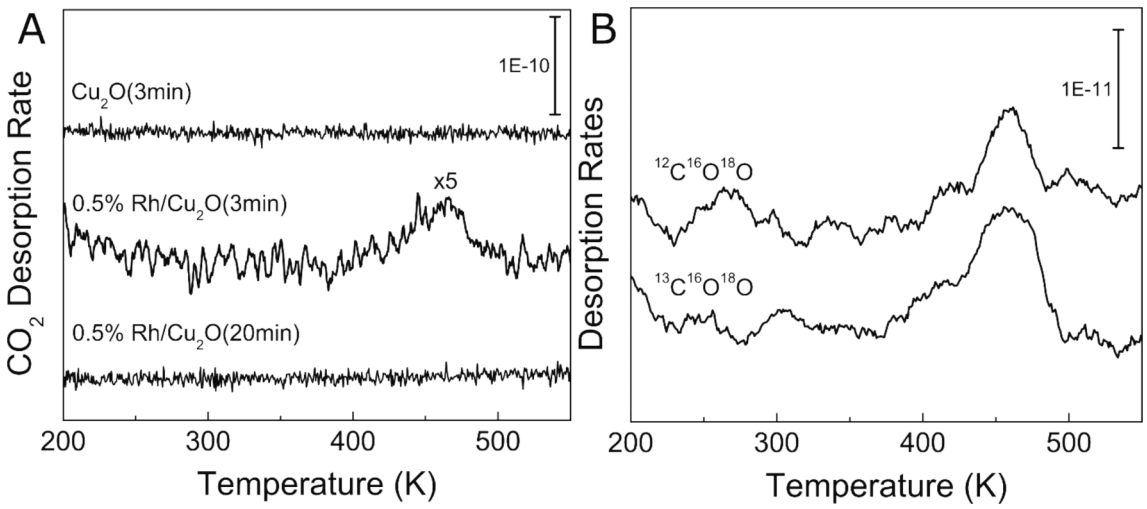


**Fig. 4.** (A) TPD data of $CO_2$ desorption from $Cu_2O$(3min), 0.5% Rh/$Cu_2O$(3min) and 0.5% Rh/$Cu_2O$(20min) after saturation $^{12}C^{16}O$ was dosed onto the surfaces at 90 K. (B) Isotopically labeled TPD data of $CO_2$ desorption from 0.5% Rh/$Cu_2O$(3min) prepared using $^{18}O_2$, showing traces of $^{12}C^{16}O^{18}O$ (top) and $^{13}C^{16}O^{18}O$ (bottom) desorption after saturation $^{13}C^{16}O$ exposure at 90 K. Both Rh/$Cu_2O$ surfaces were prepared by oxidizing RhCu SAA for the indicated times.

defective $Cu_2O$ film after the 3-minute oxidation, and these exposed Rh sites are active in CO oxidation. Moreover, oxidizing a 0.5% ML RhCu SAA for 20 min prevents any CO oxidation, as shown by the absence of any $CO_2$ desorption in the bottom trace in Fig. 4A, similar to that of the pristine $Cu_2O$(3min) surface. In this case, the Rh/$Cu_2O$(20min) surface was prepared with $^{16}O_2$, and saturation $^{12}C^{16}O$ was exposed to the surface at 90 K. The lack of a $^{12}C^{16}O^{16}O$ desorption peak indicates that CO oxidation does not occur on this system. The TPD data are consistent with the XPS data shown in Fig. 3, which demonstrate that some Rh atoms are accessible to CO in the Rh/$Cu_2O$(3min) sample but not for the Rh/$Cu_2O$(20min) sample. Together, our XPS and TPD results confirm that the 20-minute oxidation procedure produces an oxide film that covers all the Rh sites, which can neither adsorb nor oxidize CO, whereas the 3-minute oxidation of the Rh/Cu SAA leaves ~20% of the Rh sites exposed and able to adsorb and oxidize CO. The adsorption of CO on exposed Rh sites consequently leads to a slow down in the rate of $Cu_2O$ reduction in 1 Torr $H_2$ when any trace amount (UHV background) of CO is present.

Unlike PtCu SAAs, which were previously shown to bind CO weakly with a desorption temperature of ~350 K [67], the RhCu SAA binds CO at the Rh sites strongly with a desorption temperature of ~470 K [68,69], and, therefore, the Rh sites are likely to be more susceptible to CO poisoning. To examine this effect on the $Cu_2O$ reduction by $H_2$, we performed a series of experiments to observe the effect of CO pre-exposure on the reduction kinetics of the $Cu_2O$ surfaces, the results of which are shown in Fig. 5. For the Rh/$Cu_2O$(3min) surface (Fig. 5A), the reduction rate is slightly slower with CO pre-exposure, indicating the effect of CO poisoning of the exposed Rh sites. However, as demonstrated from the XPS and TPD data described above, due to CO adsorption from the UHV chamber background, the exposed Rh sites on the Rh/$Cu_2O$(3min) surface are not completely CO-free at 300 K even without intentionally dosing CO, so the reduction rate is always affected by background CO poisoning of at least half of the exposed Rh sites. On the other hand, the rapid reduction kinetics of the Rh/$Cu_2O$(20min) surface are not affected by CO poisoning, as can be seen in Fig. 5B. This intriguing result indicates that although Rh sites under the $Cu_2O$(20min) are not accessible for CO poisoning, and TPD does not show evidence for $H_2$ dissociation at UHV exposures, they are accessible to $H_2$ adsorption and active for $H_2$ dissociation at near-ambient pressure conditions. This is in contrast to Pt/$Cu_2O$(20min), which was both inaccessible for CO adsorption and inactive for $H_2$ dissociation [45].

We therefore conclude that Rh provides active sites for $H_2$

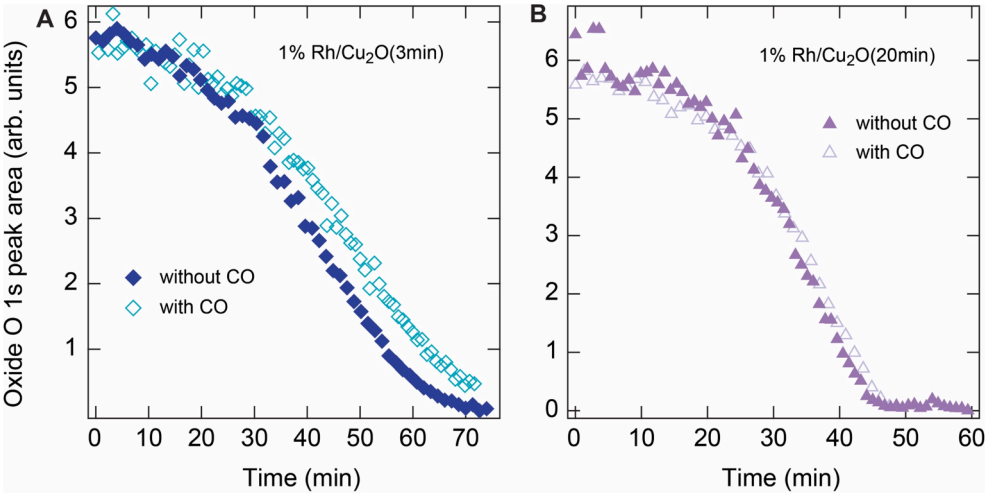


**Fig. 5.** XPS-derived plots of oxide O 1 s peak area as a function of exposure time in 1 Torr of $H_2$ at 300 K for (A) 1% Rh/$Cu_2O$(3min) and (B) 1% Rh/$Cu_2O$(20min) examining CO poisoning effects by exposing the samples to $1 \times 10^{-4}$ Torr of CO for 30 s at 300 K prior to the introduction to 1 Torr of $H_2$.

dissociation that are responsible for the rapid reduction of the $Rh/Cu_2O$ surfaces, as illustrated schematically in Fig. 6. The $Rh/Cu_2O$(20min) sample (Fig. 6A) likely has one type of active site: Rh atoms under the oxide, which are not accessible to CO, but which can adsorb and dissociate $H_2$ at elevated pressures, resulting in a significantly more rapid reduction of the oxide compared to the Rh-free sample. On the other hand, the $Rh/Cu_2O$(3min) sample (Fig. 6B) has two types of Rh sites: Rh sites under patches of oxide, which are inaccessible to CO, similar to the case for the $Rh/Cu_2O$(20min), which constitute the majority of active Rh sites for $H_2$ dissociation, and some exposed Rh sites, likely in exposed defects in the incomplete 3-minute oxide layer. These exposed Rh atoms should be able to dissociate $H_2$, but they are easily poisoned by trace amounts of CO, which consequently decreases the overall number of Rh atoms that can activate $H_2$. This provides an explanation for why the reduction of the $Rh/Cu_2O$(3min) surface in $H_2$ proceeds at a slightly slower rate than the $Rh/Cu_2O$(20min) sample in which the Rh atoms are inaccessible to CO.

### 3.2. DFT results

In order to further understand these effects, we performed DFT calculations on model surfaces. Specifically, CI-NEB VASP calculations were performed to analyze the energetics of hydrogen dissociation with Rh existing either as a single atom or in a cluster under the model $Cu_2O$ surface. Here we choose the Rh cluster to be located under an oxide ring with no O adatoms to be able to compare our results to our previous work on Pt [45] where the cluster is also located under an oxide ring with no O adatoms. In addition, we have tested the possibility of Rh being embedded in the oxide layer itself. However, as shown in the calculations that are shown in Figure S2, S3 and S4, it is more favorable for the Rh cluster to remain embedded in the Cu(111) surface rather than in the oxide layer.

Fig. 7 elucidates the dissociative pathways for $H_2$. Our DFT-based model reveals that the rate-determining step for both surfaces is adsorption of the $H_2$ at the Rh site under the oxide. As seen from Fig. 7, $H_2$ adsorption barriers for Rh atoms and clusters range from 0.29 eV to 0.42 eV. Furthermore, the $H_2$ adsorption barrier mainly lies in the adsorption process as it is difficult for $H_2$ to access the Rh underneath the thin oxide layer. Indeed, once the barrier for adsorption is overcome, the dissociation of the adsorbed $H_2$ is completely barrierless. This result is consistent with the experimental results, which show rapid reduction of the oxide layer at elevated $H_2$ pressures in the AP-XPS measurements, but no $H_2$ dissociation is observed under UHV conditions due to the aforementioned $H_2$ adsorption barriers.

The exothermic dissociative adsorption of $H_2$ on Rh under the oxide is in contrast with what we previously found for Pt, where the reaction is endothermic on Pt atoms and clusters under the oxide [45]. In addition, the $H_2$ adsorption barriers on Rh under the oxide (either as an isolated Rh atom or in clusters) are systematically lower as compared to those on Pt under the oxide by about 0.1 eV (see Table 1). These findings are also consistent with the AP-XPS measurements for which the reduction of the oxide is found to proceed more rapidly for Rh as compared to Pt, as shown in Fig. 2.

Furthermore, since CO binds more strongly to Rh than to Pt [70,71], these sites are more easily poisoned as compared to Pt, which makes previously exposed Rh sites inaccessible to $H_2$ due to CO adsorption. The stronger CO adsorption on exposed Rh as compared to Pt also explains why a defective $Cu_2O$ surface with exposed Pt atoms can dissociate $H_2$ under UHV conditions [45], while a surface with exposed Rh atoms cannot. On the other hand, the presence of a complete (20min) oxide layer over the Rh sites protects the active sites from CO adsorption, thus enabling $H_2$ dissociation and faster reduction of the oxide. Indeed, the adsorption energy of CO on a Rh SAA on Cu(111) with a protective oxide layer is much weaker as compared to when CO adsorbs on a Rh SAA that is not covered by an oxide layer. We find an adsorption energy of −1.16 eV in the presence of the oxide layer (for which the corresponding structure is shown in Figure S5), which is much weaker when compared to its reported value of −1.71 eV in the absence of the oxide layer [72]. Although an adsorption energy value of −1.16 eV is not insignificant, it is also weaker than what was found for atomically dispersed Pt on the "29" oxide (−1.27 eV) for which CO was shown to not poison the surface at 300 K since the conversion of CO to $CO_2$ was found to occur at this temperature [71]. Therefore, the Rh sites under the oxide are not poisoned by CO and remain accessible to $H_2$ adsorption, particularly at near ambient pressure conditions, and the activation of $H_2$ is exothermic (Fig. 7 and in Table 1) on both isolated Rh atoms and Rh clusters under

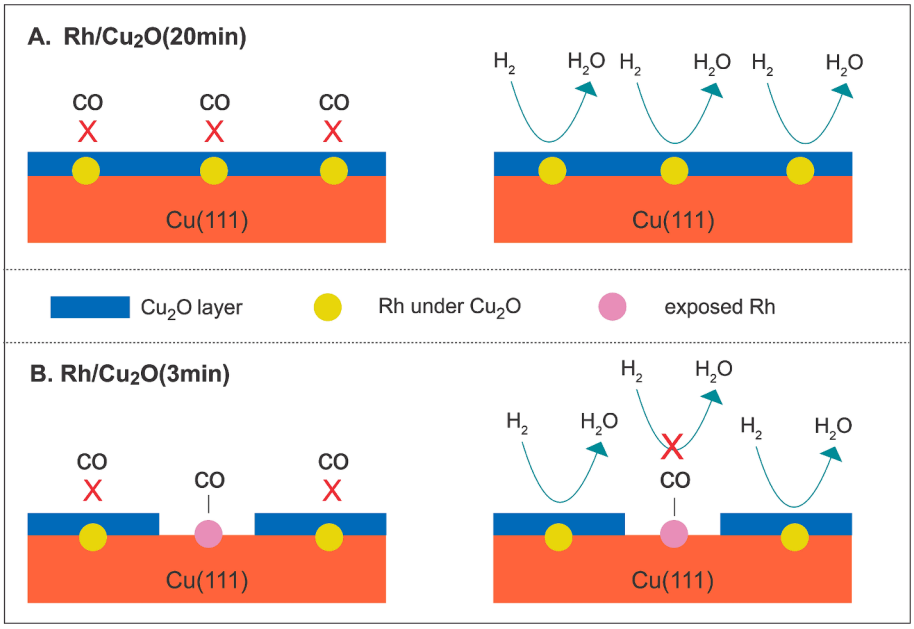


**Fig. 6.** Illustrations depicting the two cases of oxidized RhCu SAA: (A) after 20-minute oxidation, $Rh/Cu_2O$(20min), and (B) after 3-minute oxidation, $Rh/Cu_2O$(3min). The Rh sites in the 20-minute sample are inaccessible to CO but active for $H_2$ dissociation at elevated $H_2$ pressures. In contrast, for the 3-minute sample, some of the exposed Rh atoms are accessible to, and can be poisoned by, CO, while the buried Rh sites are active for $H_2$ dissociation and promote the oxide layer reduction.

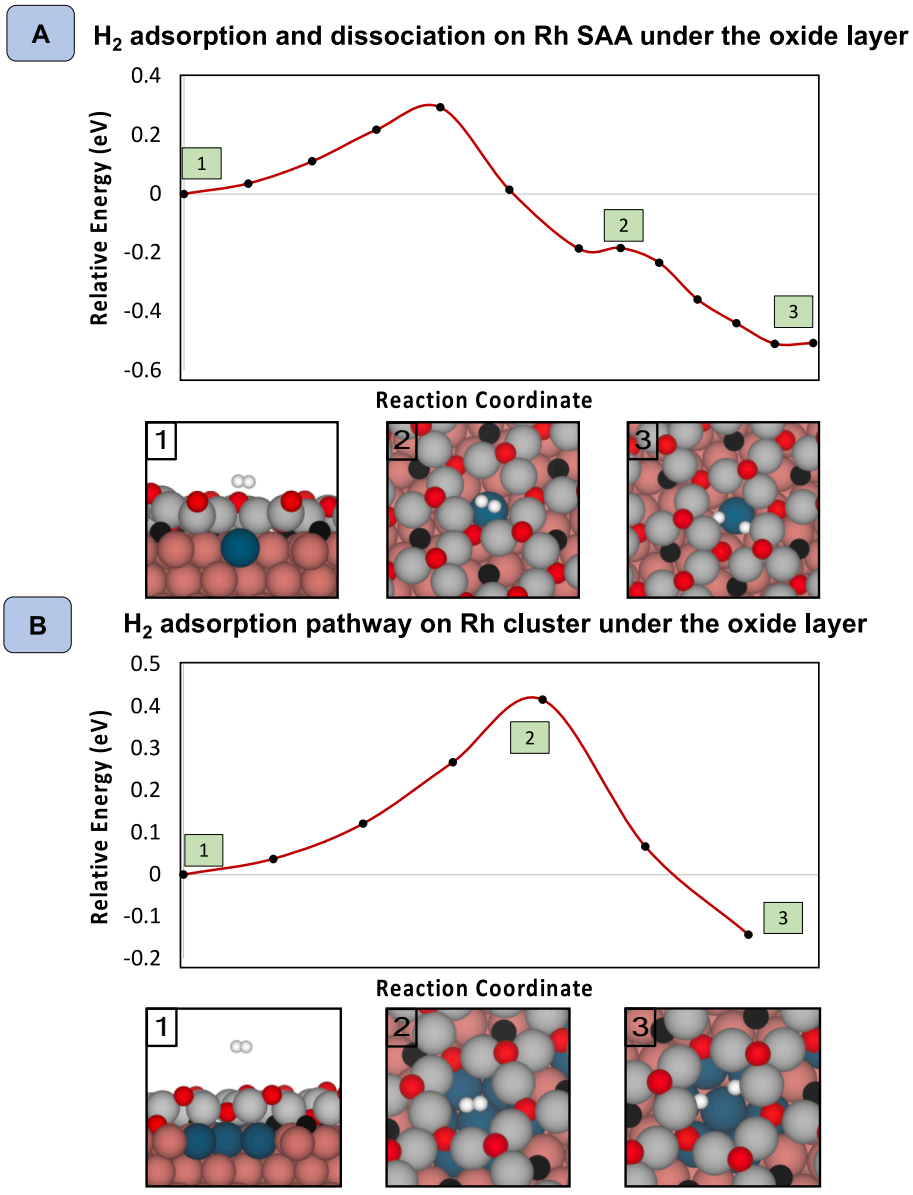


**Fig. 7.** CI-NEB pathways for $H_2$ dissociation for (A) an atomically dispersed Rh under the oxide layer and (B) a Rh cluster under the oxide layer. The red and grey spheres represent the O anion and the Cu cation in the $Cu_xO$ layer, respectively. The black and pink spheres represent the O adatoms and the Cu atoms on the Cu(111) substrate, respectively. Finally, the blue and the white spheres are the Rh and H atoms, respectively.

**Table 1**
Comparison of the activation barriers and reactions energies for Rh and Pt that form an alloy with the Cu(111) surface in which the "29" oxide is grown over it.

| Location | Rh | Pt |
|---|---|---|
| SAA Under the Oxide Layer | • *Exothermic* $\Delta E \approx -0.51$ eV<br>• Adsorption Barrier ≈ 0.29 eV<br>Most of the $H_2$ dissociation barrier lies in the adsorption process | • *Endothermic* $\Delta E \approx 0.08$ eV<br>• Adsorption Barrier ≈ 0.40 eV [45] |
| Alloy Cluster Under the Oxide Layer | • *Exothermic* $\Delta E \approx -0.14$ eV<br>• Adsorption Barrier ≈ 0.42 eV<br>• When adsorbed to the surface, $H_2$ dissociation is completely barrierless<br>Most of the $H_2$ dissociation barrier lies in the adsorption process | • *Endothermic* $\Delta E \approx 0.08$ eV<br>• Adsorption Barrier ≈ 0.50 eV [45]<br>• Barriers for both $H_2$ adsorption and dissociation |

the oxide layer.

## 4. Conclusions

In this contribution, we integrated UHV-TPD and AP-XPS measurements with first principles-based calculations to determine the influence of Rh atoms at the copper metal-oxide interface, their role in activating $H_2$, and the effect of CO poisoning. The UHV results indicate that both partial and complete $Cu_2O$ layers, prepared by oxidizing a RhCu SAA, cannot dissociate $H_2$ likely due to the adsorption of $H_2$ being activated when Rh is located under the $Cu_2O$ layer, as was found from our first principles-based model, and the unavoidable poisoning of exposed Rh sites by background CO, as demonstrated by XPS and TPD results. However, the AP-XPS results indicate that the activated adsorption of $H_2$ can be overcome at high enough pressures of $H_2$. Further, our first principles-based calculations show that once the activated adsorption of $H_2$ is overcome, the dissociation of adsorbed $H_2$ by Rh is exothermic. We experimentally demonstrated this using AP-XPS, which shows a rapid

reduction of the $Cu_2O$ thin-film by an elevated pressure of $H_2$, especially for a complete oxide layer with no exposed Rh sites that can be poisoned by CO. Interestingly, our DFT results also indicate that the dissociative adsorption of $H_2$ on the thin oxide film is more exothermic when the oxide layer covers an isolated Rh atom embedded within the underlying Cu(111) surface as compared to a cluster of Rh atoms. These results are contrasted with analogous $Cu_2O$ thin films with Pt atoms underneath, for which DFT predicts an endothermic dissociative adsorption of $H_2$ and AP-XPS shows a much slower reduction of the oxide in the absence of exposed Pt. This work demonstrates how Rh and Pt at the metal/oxide interface affect the reducibility of the thin film oxide differently in copper-based catalysts. The observation of Rh sites that remain active for $H_2$ activation even when covered by an oxide layer, and in fact the oxide layer likely protects the Rh sites from CO poisoning, has wide implications in the design of efficient hydrogenation catalysts with active metal-oxide interfaces that are resistant to the deactivating effects of both CO poisoning and encapsulation of active sites by strong metal-support interaction.

## CRediT authorship contribution statement

**Volkan Çınar:** Writing – review & editing, Writing – original draft, Investigation, Formal analysis. **Eva Peurrung:** Writing – review & editing, Writing – original draft, Investigation, Formal analysis. **Hojoon Lim:** Writing – review & editing, Investigation. **Adrian Hunt:** Writing – review & editing, Investigation. **Maggie Rickman:** Writing – review & editing, Investigation. **Grace Miller:** Writing – review & editing, Investigation. **Jean-Sabin McEwen:** Writing – review & editing, Supervision, Funding acquisition, Conceptualization. **E. Charles H. Sykes:** Writing – review & editing, Supervision, Funding acquisition, Conceptualization. **Iradwikanari Waluyo:** Writing – review & editing, Writing – original draft, Supervision, Investigation, Funding acquisition, Formal analysis, Conceptualization.

## Declaration of competing interest

The authors declare that they have no known competing financial interests or personal relationships that could have appeared to influence the work reported in this paper.

## Data availability

Data will be made available on request.

## Acknowledgements

This research used resources of the 23-ID-2 (IOS) beamline of the National Synchrotron Light Source II, a U.S. Department of Energy (DOE) Office of Science User Facility operated for the DOE Office of Science by Brookhaven National Laboratory under Contract No. DE-SC0012704. Financial support for the theoretical work at Washington State University was provided by the National Science Foundation CAREER program under contract No. CBET-1653561. Financial support for the experimental work at Tufts University was provided by the US Department of Energy, BES, Catalysis Science program under contract No. DE-SC0021196. Computational resources were provided by the Kamiak HPC under the Center for Institutional Research Computing at Washington State University. PNNL is a multi-program national laboratory operated for the US DOE by Battelle.

## Appendix A. Supplementary data

Supplementary data to this article can be found online at https://doi.org/10.1016/j.jcat.2024.115779.

## References

[1] F.D. Gunstone, F.A. Norris, Margarines and Shortenings, in: F.D. Gunstone, F. A. Norris (Eds.), Lipids in Foods, Pergamon, 1983, pp. 147–155.
[2] N.B. Johnson, I.C. Lennon, P.H. Moran, J.A. Ramsden, Industrial-scale synthesis and applications of asymmetric hydrogenation catalysts, Acc. Chem. Res. 40 (2007) 1291–1299, https://doi.org/10.1021/ar700114k.
[3] R.N. Landau, U. Singh, F. Gortsema, Y.K. Sun, S.C. Gomolka, T. Lam, M. Futran, D. G. Blackmond, A reaction calorimetric investigation of the hydrogenation of a substituted pyrazine, J. Catal. 157 (1995) 201–208, https://doi.org/10.1006/jcat.1995.1280.
[4] M. Bouchy, S. Peureuxdenys, P. Dufresne, S. Kasztelan, Hydrogenation and hydrocracking of a model light cycle oil feed. 2. Properties of a sulfided nimo hydrocracking catalyst, Ind. Eng. Chem. Res. 32 (1993) 1592–1602, https://doi.org/10.1021/ie00020a010.
[5] A.T. Lapinas, M.T. Klein, B.C. Gates, A. Macris, J.E. Lyons, Catalytic-hydrogenation and hydrocracking of fluorene - reaction pathways, kinetics, and mechanisms, Ind. Eng. Chem. Res. 30 (1991) 42–50, https://doi.org/10.1021/ie00049a007.
[6] F. Zaera, Selectivity in hydrocarbon catalytic reforming: a surface chemistry perspective, Appl. Catal. A. Gen. 229 (2002) 75–91, https://doi.org/10.1016/S0926-860x(02)00017-0.
[7] U.K. Singh, M.A. Vannice, Kinetics of liquid-phase hydrogenation reactions over supported metal catalysts - a review, Appl. Catal. A. Gen. 213 (2001) 1–24, https://doi.org/10.1016/S0926-860x(00)00885-1.
[8] M. Pan, A.J. Brush, Z.D. Pozun, H.C. Ham, W.Y. Yu, G. Henkelman, G.S. Hwang, C. B. Mullins, Model studies of heterogeneous catalytic hydrogenation reactions with gold, Chem. Soc. Rev. 42 (2013) 5002–5013, https://doi.org/10.1039/c3cs35523c.
[9] R.P. Ye, J. Ding, W.B. Gong, M.D. Argyle, Q. Zhong, Y.J. Wang, C.K. Russell, Z. H. Xu, A.G. Russell, Q.H. Li, M.H. Fan, Y.G. Yao, $CO_2$ hydrogenation to high-value products via heterogeneous catalysis, Nat. Commun. 10 (2019) 5698, https://doi.org/10.1038/s41467-019-13638-9.
[10] M. Irfan, T.N. Glasnov, C.O. Kappe, Heterogeneous catalytic hydrogenation reactions in continuous-flow reactors, ChemSusChem. 4 (2011) 300–316, https://doi.org/10.1002/cssc.201000354.
[11] M.A. Stoffels, F.J.R. Klauck, T. Hamadi, F. Glorius, J. Leker, Technology trends of catalysts in hydrogenation reactions: a patent landscape analysis, Adv. Synth. Catal. 362 (2020) 1258–1274, https://doi.org/10.1002/adsc.201901292.
[12] L. Alig, M. Fritz, S. Schneider, First-row transition metal (de)hydrogenation catalysis based on functional pincer ligands, Chem. Rev. 119 (2019) 2681–2751, https://doi.org/10.1021/acs.chemrev.8b00555.
[13] F. Cárdenas-Lizana, M.A. Keane, The development of gold catalysts for use in hydrogenation reactions, J. Mater. Sci. 48 (2013) 543–564, https://doi.org/10.1007/s10853-012-6766-7.
[14] M.D. Navalikhina, O.V. Krylov, Heterogeneous catalysts of hydrogenation, Russ. Chem. Rev. 67 (1998) 587–616, https://doi.org/10.1070/RC1998v067n07ABEH000413.
[15] R.J. Liu, P.A. Crozier, C.M. Smith, D.A. Hucul, J. Blackson, G. Salaita, Metal sintering mechanisms and regeneration of palladium/alumina hydrogenation catalysts, Appl. Catal. A. Gen. 282 (2005) 111–121, https://doi.org/10.1016/j.apcata.2004.12.015.
[16] L.L. Lin, J.J. Liu, X. Liu, Z.R. Gao, N. Rui, S.Y. Yao, F. Zhang, M.L. Wang, C. Liu, L. L. Han, F. Yang, S. Zhang, X.D. Wen, S.D. Senanayake, Y.C. Wu, X.N. Li, J. A. Rodriguez, D. Ma, Reversing sintering effect of Ni particles on γ-$Mo_2N$ via strong metal support interaction, Nat. Commun. 12 (2021) 6978, https://doi.org/10.1038/s41467-021-27116-8.
[17] Z. Li, N.M. Schweitzer, A.B. League, V. Bernales, A.W. Peters, A. Getsoian, T. C. Wang, J.T. Miller, A. Vjunov, J.L. Fulton, J.A. Lercher, C.J. Cramer, L. Gagliardi, J.T. Hupp, O.K. Farha, Sintering-resistant single-site nickel catalyst supported by metal organic framework, J. Am. Chem. Soc. 138 (2016) 1977–1982, https://doi.org/10.1021/jacs.5b12515.
[18] F. Wang, J.C. Zhang, W.Z. Li, B.H. Chen, Coke-resistant Au-Ni/$MgAl_2O_4$ catalyst for direct methanation of syngas, J. Energy Chem. 39 (2019) 198–207, https://doi.org/10.1016/j.jechem.2019.03.028.
[19] J. Barbier, Deactivation of reforming catalysts by coking - a review, Appl. Catal. 23 (1986) 225–243, https://doi.org/10.1016/S0166-9834(00)81294-4.
[20] S.S. Xu, S. Chansai, S.J. Xu, C.E. Stere, Y.L. Jiao, S.H. Yang, C. Hardacre, X.L. Fan, CO poisoning of Ru catalysts in $CO_2$ hydrogenation under thermal and plasma conditions: a combined kinetic and diffuse reflectance infrared fourier transform spectroscopy-mass spectrometry study, ACS Catal. 10 (2020) 12828–12840, https://doi.org/10.1021/acscatal.0c03620.
[21] J. Grunes, J. Zhu, M.C. Yang, G.A. Somorjai, CO poisoning of ethylene hydrogenation over Pt catalysts: a comparison of Pt(111) single crystal and Pt nanoparticle activities, Catal. Lett. 86 (2003) 157–161, https://doi.org/10.1023/A:1022628404888.
[22] E. Guan, L. Debefve, M. Vasiliu, S.J. Zhang, D.A. Dixon, B.C. Gates, MgO-supported iridium metal pair-site catalysts are more active and resistant to CO poisoning than analogous single-site catalysts for ethylene hydrogenation and hydrogen-deuterium exchange, ACS Catal. 9 (2019) 9545–9553, https://doi.org/10.1021/acscatal.9b03463.
[23] L.L. Lin, S.Y. Yao, R. Gao, X. Liang, Q.L. Yu, Y.C. Deng, J.J. Liu, M. Peng, Z. Jiang, S.W. Li, Y.W. Li, X.D. Wen, W. Zhou, D. Ma, A highly CO-tolerant atomically dispersed Pt catalyst for chemoselective hydrogenation, Nat. Nanotechnol. 14 (2019) 354–361, https://doi.org/10.1038/s41565-019-0366-5.
[24] Y.L. Guo, Y.K. Huang, B. Zeng, B. Han, M. Akri, M. Shi, Y. Zhao, Q.H. Li, Y. Su, L. Li, Q.K. Jiang, Y.T. Cui, L. Li, R.G. Li, B.T. Qiao, T. Zhang, Photo-thermo semi-

hydrogenation of acetylene on $Pd_1/TiO_2$ single-atom catalyst, Nat. Commun. 13 (2022) 2648, https://doi.org/10.1038/s41467-022-30291-x.
[25] H.F. Qi, J. Yang, F. Liu, L.L. Zhang, J.Y. Yang, X.Y. Liu, L. Li, Y. Su, Y.F. Liu, R. Hao, A.Q. Wang, T. Zhang, Highly selective and robust single-atom catalyst $Ru_1$/NC for reductive amination of aldehydes/ketones, Nat. Commun. 12 (2021) 3295, https://doi.org/10.1038/s41467-021-23429-w.
[26] W.G. Liu, Y.J. Chen, H.F. Qi, L.L. Zhang, W.S. Yan, X.Y. Liu, X.F. Yang, S. Miao, W. T. Wang, C.G. Liu, A.Q. Wang, J. Li, T. Zhang, A durable nickel single-atom catalyst for hydrogenation reactions and cellulose valorization under harsh conditions, Angew. Chem. Int. Ed. 57 (2018) 7071–7075, https://doi.org/10.1002/anie.201802231.
[27] Z.J. Li, X.L. Dong, M.Y. Zhang, L.P. Leng, W.X. Chen, J.H. Horton, J. Wang, W. Wu, Selective hydrogenation on a highly active single-atom catalyst of palladium dispersed on ceria nanorods by defect engineering, ACS Appl. Mater. Inter. 12 (2020) 57569–57577, https://doi.org/10.1021/acsami.0c17009.
[28] Z.J. Li, M.Y. Zhang, X.L. Dong, S.Q. Ji, L.L. Zhang, L.P. Leng, H.H. Li, J.H. Horton, Q. Xu, J.F. Zhu, Strong electronic interaction of indium oxide with palladium single atoms induced by quenching toward enhanced hydrogenation of nitrobenzene, Appl. Catal. B Environ. 313 (2022) 121462, https://doi.org/10.1016/j.apcatb.2022.121462.
[29] S.J. Tauster, S.C. Fung, R.T.K. Baker, J.A. Horsley, Strong-interactions in supported-metal catalysts, Science 211 (1981) 1121–1125, https://doi.org/10.1126/science.211.4487.1121.
[30] J.P.S. Badyal, Strong Metal-Support Interactions, in: D.A. King, D.P. Woodruff (Eds.), The Chemical Physics of Solid Surfaces, Elsevier, 1993, pp. 311–340.
[31] S.J. Tauster, Strong metal-support interactions, Acc. Chem. Res. 20 (1987) 389–394, https://doi.org/10.1021/ar00143a001.
[32] C.J. Pan, M.C. Tsai, W.N. Su, J. Rick, N.G. Akalework, A.K. Agegnehu, S.Y. Cheng, B.J. Hwang, Tuning/exploiting Strong Metal-Support Interaction (SMSI) in Heterogeneous Catalysis, J. Taiwan Inst. Chem. Eng. 74 (2017) 154–186, https://doi.org/10.1016/j.jtice.2017.02.012.
[33] S.L. Hu, W.X. Li, Sabatier principle of metal-support interaction for design of ultrastable metal nanocatalysts, Science 374 (2021) 1360–1365, https://doi.org/10.1126/science.abi9828.
[34] A. Beck, X. Huang, L. Artiglia, M. Zabilskiy, X. Wang, P. Rzepka, D. Palagin, M. G. Willinger, J.A. van Bokhoven, The dynamics of overlayer formation on catalyst nanoparticles and strong metal-support interaction, Nat. Commun. 11 (2020) 3220, https://doi.org/10.1038/s41467-020-17070-2.
[35] J. Zhang, H. Wang, L. Wang, S. Ali, C.T. Wang, L.X. Wang, X.J. Meng, B. Li, D.S. Su, F.S. Xiao, Wet-chemistry strong metal-support interactions in titania-supported Au catalysts, J. Am. Chem. Soc. 141 (2019) 2975–2983, https://doi.org/10.1021/jacs.8b10864.
[36] H.L. Tang, Y. Su, B.S. Zhang, A.F. Lee, M.A. Isaacs, K. Wilson, L. Li, Y.G. Ren, J. H. Huang, M. Haruta, B.T. Qiao, X. Liu, C.Z. Jin, D.S. Su, J.H. Wang, T. Zhang, Classical strong metal-support interactions between gold nanoparticles and titanium dioxide, Sci. Adv. 3 (2017) e170023, https://doi.org/10.1126/sciadv.1700231.
[37] Z.X. Luo, G.Q. Zhao, H.G. Pan, W.P. Sun, Strong metal-support interaction in heterogeneous catalysts, Adv. Energy. Mater. 12 (2022) 2201395, https://doi.org/10.1002/aenm.202201395.
[38] J.Q. Zhong, H.J. Freund, Two-dimensional ultrathin silica films, Chem. Rev. 122 (2022) 11172–11246, https://doi.org/10.1021/acs.chemrev.1c00995.
[39] Y.J. Liu, R.K. Zhang, L. Lin, Y.C. Wang, C.P. Liu, R.T. Mu, Q. Fu, Direct observation of accelerating hydrogen spillover via surface-lattice-confinement effect, Nat. Commun. 14 (2023) 613, https://doi.org/10.1038/s41467-023-36044-8.
[40] M.J. Prieto, T. Mullan, M. Schlutow, D.M. Gottlob, L.C. Tanase, D. Menzel, J. Sauer, D. Usvyat, T. Schmidt, H.J. Freund, Insights into reaction kinetics in confined space: real time observation of water formation under a silica cover, J. Am. Chem. Soc. 143 (2021) 8780–8790, https://doi.org/10.1021/jacs.1c03197.
[41] J.A. Rodriguez, J.Y. Kim, J.C. Hanson, M. Perez, A.I. Frenkel, Reduction of CuO in $H_2$: in situ time-resolved XRD studies, Catal. Lett. 85 (2003) 247–254, https://doi.org/10.1023/A:1022110200942.
[42] J.Y. Kim, J.A. Rodriguez, J.C. Hanson, A.I. Frenkel, P.L. Lee, Reduction of CuO and $Cu_2O$ with $H_2$: H embedding and kinetic effects in the formation of suboxides, J. Am. Chem. Soc. 125 (2003) 10684–10692, https://doi.org/10.1021/ja0301673.
[43] R.G. Zhang, B.J. Wang, L.X. Ling, H.Y. Liu, W. Huang, Adsorption and dissociation of $H_2$ on the $Cu_2O$(111) surface: a density functional theory study, Appl Surf Sci 257 (2010) 1175–1180, https://doi.org/10.1016/j.apsusc.2010.07.095.
[44] F. Xu, W. An, A.E. Baber, D.C. Grinter, S.D. Senanayake, M.G. White, P. Liu, D. J. Stacchiola, Enhanced oxide reduction by hydrogen at cuprous oxide-copper interfaces near ascending step edges, J. Phys. Chem. C 126 (2022) 18645–18651, https://doi.org/10.1021/acs.jpcc.2c03719.
[45] A.C. Schilling, K. Groden, J.P. Simonovis, A. Hunt, R.T. Hannagan, V. Çınar, J.-S. McEwen, E.C.H. Sykes, I. Waluyo, Accelerated $Cu_2O$ reduction by single Pt atoms at the metal-oxide interface, ACS Catal. 10 (2020) 4215–4226, https://doi.org/10.1021/acscatal.9b05270.
[46] I. Waluyo, A. Hunt, Ambient pressure X-ray photoelectron spectroscopy at the IOS (23-ID-2) beamline at the National Synchrotron Light Source II, Synchrotron Radiat. News 35 (2022) 31–38, https://doi.org/10.1080/08940886.2022.2082180.
[47] G. Kresse, J. Furthmuller, Efficient iterative schemes for ab initio total-energy calculations using a plane-wave basis set, Phys. Rev. B 54 (1996) 11169–11186, https://doi.org/10.1103/PhysRevB.54.11169.
[48] G. Kresse, J. Hafner, Ab initio molecular-dynamics for liquid-metals, Phys. Rev. B 47 (1993) 558–561, https://doi.org/10.1103/PhysRevB.47.558.
[49] G. Kresse, D. Joubert, From ultrasoft pseudopotentials to the projector augmented-wave method, Phys. Rev. B 59 (1999) 1758–1775, https://doi.org/10.1103/PhysRevB.59.1758.
[50] P.E. Blochl, Projector Augmented-Wave Method, Phys. Rev. B 50 (1994) 17953–17979, https://doi.org/10.1103/PhysRevB.50.17953.
[51] K. Lejaeghere, G. Bihlmayer, T. Björkman, P. Blaha, S. Blügel, V. Blum, D. Caliste, I. E. Castelli, S.J. Clark, A. Dal Corso, S. de Gironcoli, T. Deutsch, J.K. Dewhurst, I. Di Marco, C. Draxl, M. Dulak, O. Eriksson, J.A. Flores-Livas, K.F. Garrity, L. Genovese, P. Giannozzi, M. Giantomassi, S. Goedecker, X. Gonze, O. Grånäs, E.K.U. Gross, A. Gulans, F. Gygi, D.R. Hamann, P.J. Hasnip, N.A.W. Holzwarth, D. Iusan, D. B. Jochym, F. Jollet, D. Jones, G. Kresse, K. Koepernik, E. Küçükbenli, Y. O. Kvashnin, I.L.M. Locht, S. Lubeck, M. Marsman, N. Marzari, U. Nitzsche, L. Nordström, T. Ozaki, L. Paulatto, C.J. Pickard, W. Poelmans, M.I.J. Probert, K. Refson, M. Richter, G.M. Rignanese, S. Saha, M. Scheffler, M. Schlipf, K. Schwarz, S. Sharma, F. Tavazza, P. Thunström, A. Tkatchenko, M. Torrent, D. Vanderbilt, M.J. van Setten, V. Van Speybroeck, J.M. Wills, J.R. Yates, G. X. Zhang, S. Cottenier, Reproducibility in density functional theory calculations of solids, Science 351 (2016) aad3000, https://doi.org/10.1126/science.aad3000.
[52] J. Paier, R. Hirschl, M. Marsman, G. Kresse, The Perdew-Burke-Ernzerhof exchange-correlation functional applied to the G2–1 test set using a plane-wave basis set, J. Chem. Phys. 122 (2005) 234102, https://doi.org/10.1063/1.1926272.
[53] A. Stukowski, Visualization and analysis of atomistic simulation data with OVITO-the open visualization tool, Model. Simul. Mater. Sci. Eng. 18 (2010) 015012, https://doi.org/10.1088/0965-0393/18/1/015012.
[54] A.J.R. Hensley, A.J. Therrien, R.Q. Zhang, M.D. Marcinkowsi, F.R. Lucci, E.C. H. Sykes, J.-S. McEwen, CO adsorption on the "29" $Cu_2O$/Cu(111) surface: an integrated DFT, STM, and TPD study, J. Phys. Chem. C 120 (2016) 25387–25394, https://doi.org/10.1021/acs.jpcc.6b07670.
[55] A.J. Therrien, A.J.R. Hensley, R.Q. Zhang, A. Pronschinske, M.D. Marcinkowski, J.-S. McEwen, E.C.H. Sykes, Characterizing the geometric and electronic structure of defects in the "29" copper surface oxide, J. Chem. Phys. 147 (2017) 224706, https://doi.org/10.1063/1.4996729.
[56] A.J. Therrien, R.Q. Zhang, F.R. Lucci, M.D. Marcinkowski, A. Hensley, J.-S. McEwen, E.C.H. Sykes, Structurally accurate model for the "29"-structure of $Cu_2O$/Cu(111): A DFT and STM study, J. Phys. Chem. C 120 (2016) 10879–10886, https://doi.org/10.1021/acs.jpcc.6b01284.
[57] G. Henkelman, H. Jónsson, A dimer method for finding saddle points on high dimensional potential surfaces using only first derivatives, J. Chem. Phys. 111 (1999) 7010–7022, https://doi.org/10.1063/1.480097.
[58] G. Henkelman, B.P. Uberuaga, H. Jónsson, A climbing image nudged elastic band method for finding saddle points and minimum energy paths, J. Chem. Phys. 113 (2000) 9901–9904, https://doi.org/10.1063/1.1329672.
[59] S.A. Trygubenko, D.J. Wales, A doubly nudged elastic band method for finding transition states, J. Chem. Phys. 120 (2004) 2082–2094, https://doi.org/10.1063/1.1636455.
[60] F. Jensen, F. Besenbacher, I. Stensgaard, Two new oxygen induced reconstructions on Cu(111), Surf. Sci. 269 (1992) 400–404, https://doi.org/10.1016/0039-6028(92)91282-G.
[61] T. Matsumoto, R.A. Bennett, P. Stone, T. Yamada, K. Domen, M. Bowker, Scanning tunneling microscopy studies of oxygen adsorption on Cu(111), Surf. Sci. 471 (2001) 225–245, https://doi.org/10.1016/S0039-6028(00)00918-3.
[62] F. Jensen, F. Besenbacher, E. Laegsgaard, I. Stensgaard, Oxidation of Cu(111) - two new oxygen induced reconstructions, Surf. Sci. 259 (1991) L774–L780, https://doi.org/10.1016/0039-6028(91)90550-C.
[63] D.M. Shakya, O.A. Ejegbavwo, T. Rajeshkumar, S.D. Senanayake, A.J. Brandt, S. Farzandh, N. Acharya, A.M. Ebrahim, A.I. Frenkel, N. Rui, G.L. Tate, J. R. Monnier, K.D. Vogiatzis, N.B. Shustova, D.A. Chen, Selective catalytic chemistry at rhodium(II) nodes in bimetallic metal-organic frameworks, Angew. Chem. Int. Ed. 58 (2019) 16533–16537, https://doi.org/10.1002/anie.201908761.
[64] A.A. Tolia, R.J. Smiley, W.N. Delgass, C.G. Takoudis, M.J. Weaver, Surface oxidation of rhodium at ambient pressures as probed by surface-enhanced Raman and X-ray photoelectron spectroscopies, J. Catal. 150 (1994) 56–70, https://doi.org/10.1006/jcat.1994.1322.
[65] L.S. Kibis, A.I. Stadnichenko, S.V. Koscheev, V.I. Zaikovskii, A.I. Boronin, XPS study of nanostructured rhodium oxide film comprising $Rh^{4+}$ species, J. Phys. Chem. C 120 (2016) 19142–19150, https://doi.org/10.1021/acs.jpcc.6b05219.
[66] A.C. Schilling, N. Ulumuddin, V. Çınar, R.T. Hannagan, K. Groden, Y.C. Wang, L. A. Cramer, P.L. Kress, D.A. Patel, B. Vo, A. Hunt, P. Christopher, I. Waluyo, J.-S. McEwen, E.C.H. Sykes, Elucidating CO Oxidation pathways on Rh atoms and clusters on the "29" $Cu_2O$/Cu(111) surface, J. Phys. Chem. C 126 (2022) 11091–11102, https://doi.org/10.1021/acs.jpcc.2c02699.
[67] J.L. Liu, F.R. Lucci, M. Yang, S. Lee, M.D. Marcinkowski, A.J. Therrien, C. T. Williams, E.C.H. Sykes, M. Flytzani-Stephanopoulos, Tackling CO poisoning with single-atom alloy catalysts, J. Am. Chem. Soc. 138 (2016) 6396–6399, https://doi.org/10.1021/jacs.6b03339.
[68] R.T. Hannagan, D.A. Patel, L.A. Cramer, A.C. Schilling, P.T.P. Ryan, A.M. Larson, V. Çınar, Y.C. Wang, T.A. Balema, E.C.H. Sykes, Combining STM, RAIRS and TPD to decipher the dispersion and interactions between active sites in RhCu single-atom alloys, ChemCatChem 12 (2020) 488–493, https://doi.org/10.1002/cctc.201901488.
[69] R.T.T. Hannagan, Y.C. Wang, R. Reocreux, J. Schumann, M. Stamatakis, E.C. H. Sykes, Tuning the product selectivity of single-atom alloys by active site modification, Surf. Sci. 717 (2022) 121990, https://doi.org/10.1016/j.susc.2021.121990.
[70] N. Ulumuddin, V. Cinar, A.C. Schilling, A. Hunt, I. Waluyo, E.C.H. Sykes, J.-S. McEwen, Assessing factors that determine adatom migration and clustering on a

thin film oxide; $Pt_1$ and $Rh_1$ on the "29" $Cu_xO$/Cu(111) surface, Appl. Surf. Sci. 628 (2023) 157145, https://doi.org/10.1016/j.apsusc.2023.157145.
[71] A.J. Therrien, A.J.R. Hensley, M.D. Marcinkowski, R.Q. Zhang, F.R. Lucci, B. Coughlin, A.C. Schilling, J.-S. McEwen, E.C.H. Sykes, An atomic-scale view of single-site Pt catalysis for low-temperature CO oxidation, Nat. Catal. 1 (2018) 192–198, https://doi.org/10.1038/s41929-018-0028-2.
[72] M.T. Darby, E.C.H. Sykes, A. Michaelides, M. Stamatakis, Carbon monoxide poisoning resistance and structural stability of single atom alloys, Top. Catal. 61 (2018) 428–438, https://doi.org/10.1007/s11244-017-0882-1.